

QUANTUM OPTICS

A topological quantum optics interface

Sabyasachi Barik,^{1,2} Aziz Karasahin,³ Christopher Flower,^{1,2} Tao Cai,³
Hirokazu Miyake,² Wade DeGottardi,^{1,2} Mohammad Hafezi,^{1,2,3*} Edo Waks^{1,2,3*}

The application of topology in optics has led to a new paradigm in developing photonic devices with robust properties against disorder. Although considerable progress on topological phenomena has been achieved in the classical domain, the realization of strong light-matter coupling in the quantum domain remains unexplored. We demonstrate a strong interface between single quantum emitters and topological photonic states. Our approach creates robust counterpropagating edge states at the boundary of two distinct topological photonic crystals. We demonstrate the chiral emission of a quantum emitter into these modes and establish their robustness against sharp bends. This approach may enable the development of quantum optics devices with built-in protection, with potential applications in quantum simulation and sensing.

The discovery of the quantum Hall effects has inspired developments in similar topological phenomena in a range of platforms, including ultracold neutral atoms (1, 2), photonics (3, 4), and mechanical structures (5–7). Like their electronic analogs, topological photonic states are distinctive in their directional transport and reflectionless propagation along the interface of two topologically distinct regions. Such robustness has been demonstrated in various electromagnetic systems, ranging from the microwave (8, 9) to the optical (10, 11) domain, opening avenues for a plethora of applications—such as robust delay lines, slow-light optical buffers (12), and topological lasers (13–15)—to develop optical devices with built-in protection. Although the scope of previous work has remained in the classical electromagnetic regime, interesting physics could emerge by bringing topological photonics to the quantum domain. Specifically, integrating quantum emitters into topological photonic structures could lead to robust, strong light-matter interaction (16) and the generation of novel states of light and exotic many-body states (17–19).

We experimentally demonstrated light-matter coupling in a topological photonic crystal. We used an all-dielectric structure (20–22) to implement topologically robust edge states at the interface between two topologically distinct photonic materials, where the light is transversally trapped in a small area, up to half of the wavelength of light. We show that a quantum emitter efficiently couples to these edge modes and that the emitted single photons exhibit robust transport, even in

the presence of a bend. Figure 1A shows the fabricated topological photonic crystal structure. The device is composed of a thin GaAs membrane with epitaxially grown InAs quantum dots at the center that act as quantum emitters (22).

The topological photonic structure comprises two deformed honeycomb photonic crystal lattices made of equilateral triangular air holes (fig. S2) on a GaAs membrane (21, 22). Figure 1B shows a close-up image of the interface, where the black dashed lines identify a single unit cell of each photonic crystal. In each region, we perturb the unit cell by concentrically moving the triangular holes either inward (yellow region) or outward (blue region). The corresponding band structures of the two regions are shown in Fig. 1, C and D. The perturbations open two bandgaps exhibiting band inversion at the Γ point (20, 21).

Specifically, the region with a compressed unit cell, highlighted in yellow, acquires a topologically trivial bandgap, whereas the expanded region, highlighted in blue, takes on a nontrivial one. We designed both regions so that their bandgaps overlap. Photons within the common bandgap cannot propagate into either photonic crystal. However, because the crystals have different topological band properties, the interface between them supports two topological helical edge modes, traveling in opposite directions, with opposite circular polarizations at the center of the unit cell.

To show the presence of the guided edge mode, we measured the transmission spectrum. We illuminated the left grating (“L”) with a 780-nm continuous-wave laser using a pump power of 1.3 μ W and collected the emission from the right grating (“R”; Fig. 2A). At this power, the quantum dot ensemble emission became a broad continuum owing to power broadening, resulting in an internal white light source that spanned the wavelength range of 900 to 980 nm. Figure 2B shows the spectrum at the right grating, presented with the band structure simulation (21). Light emitted within the topological band efficiently transmitted through the edge mode and propagated to the other grating coupler, whereas photons outside of the bandgap dissipated into bulk modes.

To confirm that the emission originates from guided modes at the interface between the two topological materials, we excited the structure in the middle of the waveguide (“M”) and collected the emission at the left and right grating coupler, which we independently calibrated (22). Figure 2C shows the transmission spectrum collected from the left coupler as a function of the laser spot position as we scanned the laser along the y axis (across the interface indicated by the blue arrow in Fig. 2A). The spectrum attained a maximum transmission within the topological band when the pump excited the center of the structure. When

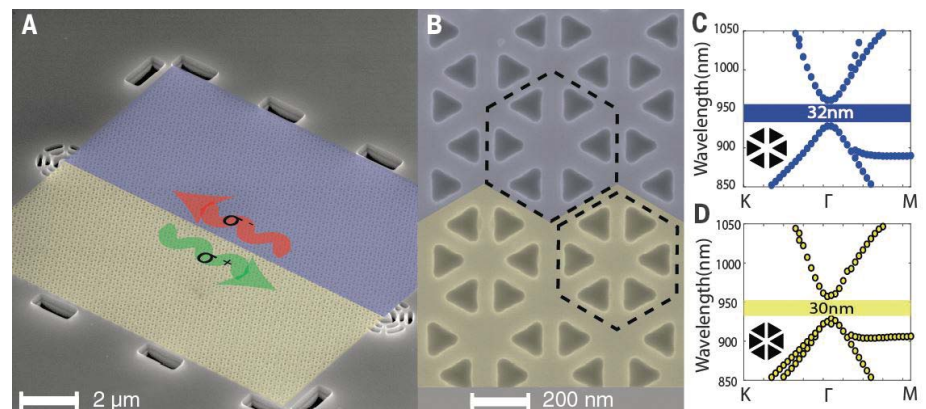


Fig. 1. Fabricated device and band structure. (A) Scanning electron microscope image of the device, which is composed of two regions identified by blue and yellow shading, corresponding to two photonic crystals with different topological properties. The interface between the two photonic crystals supports helical edge states with opposite circular polarization (σ^+ and σ^-). Grating couplers at each end of the device scatter light in the out-of-plane direction for collection. (B) Close-up image of the interface. Black dashed lines identify a single unit cell of each photonic crystal. (C and D) Band structures for the transverse electric modes of the two photonic crystals.

¹Department of Physics, University of Maryland, College Park, MD 20742, USA. ²Joint Quantum Institute, University of Maryland, College Park, MD 20742, USA. ³Department of Electrical and Computer Engineering and Institute for Research in Electronics and Applied Physics, University of Maryland, College Park, MD 20742, USA.

*Corresponding author. Email: hafezi@umd.edu (M.H.); edowaks@umd.edu (E.W.)

we displaced the excitation beam by $\sim 1.5 \mu\text{m}$ along the y direction, the transmission vanished, indicating that the photons were coming only from the waveguide.

A key feature of topological edge modes is the chiral nature of the coupling between the helical topological edge mode and the quantum emitter. Specifically, different dipole spins radiatively couple to opposite propagating helical edge states. To demonstrate this helical light-matter coupling, we applied a magnetic field in the out-of-plane (Faraday) direction on the entire sample. This field induced a Zeeman splitting in the quantum dot excited state, resulting in two nondegenerate states that emitted with opposite circular polarizations (fig. S5), denoted as σ^\pm (Fig. 3A) (22, 23). Although this magnetic field does not play a role in the topological nature of the waveguide, it enabled us to identify the polarization of the dipole by the frequency of emitted photons. By spectrally resolving the emissions, we were able to identify the dipole spin and correlate it with the propagation direction of the emitted photon.

To isolate a single quantum emitter within the topological edge mode, we reduced the power to 10 nW, which is well below the quantum dot saturation power. Using the intensities of the collected light at the two ends, we calculated a lower bound on the coupling efficiency of 68% (table S1), defined as the ratio of the photon emission rate into the waveguide to the total emission rate (22). This high efficiency is due to the tight electromagnetic confinement of the guided modes, which enhances light-matter interactions. Figure 3B shows the emission spectrum as a function of magnetic field, where we collected the emission directly from point M indicated in Fig. 2A. As the magnetic field increases, the quantum dot resonance splits into two branches corresponding to the two Zeeman split bright exciton states. We compared this spectrum with the one collected from the left and right gratings (Fig. 3, C and D). At the left grating, we observed only the emission from the σ^- branch, whereas at the right grating, we observed only the emission from the σ^+ branch. These results establish the chiral emission and spin-momentum locking of the emitted photons and provide strong evidence that the emitter is coupling to topological edge states that exhibit unidirectional transport. Such chiral coupling is in direct analogy to one-dimensional systems (16, 24, 25); however, the waveguided modes of our structure originate from two-dimensional topology. As a result, the topological edge mode should exhibit robustness to certain deformations, such as bends.

To establish this topological robustness, we analyzed the propagation of emitted photons in the presence of a bend. We introduced a 60° bend into the structure, as shown in Fig. 4A, and performed measurements similar to those in Fig. 3. Again, we observed that emitted photons propagate in opposite directions in a chiral fashion and arrive at the grating associated with their respective polarization (Fig. 4, B and C). The preservation of the chiral nature of the emission

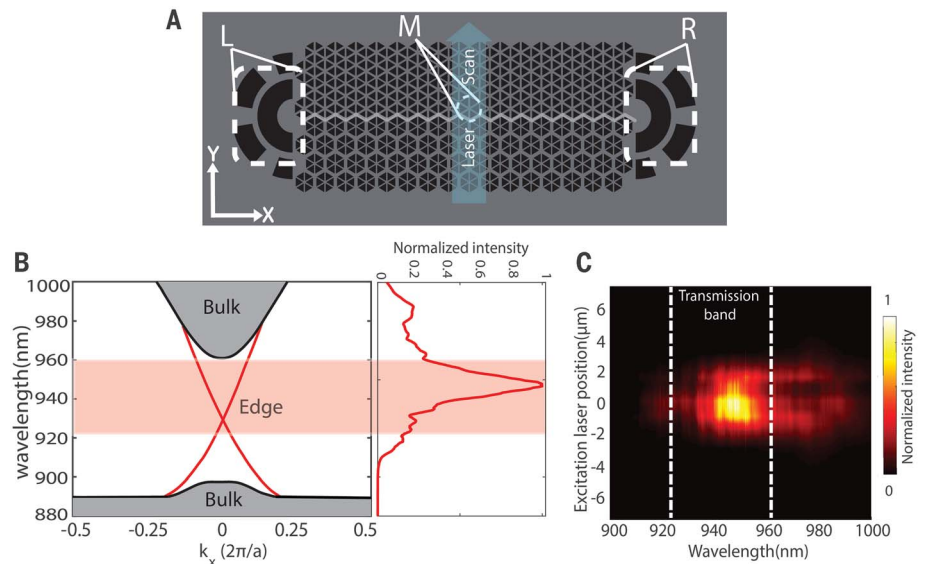


Fig. 2. Transmission characteristics of the topological waveguide. (A) A schematic of the excitation scheme identifying the three relevant regions (L, left grating; R, right grating; M, middle of the waveguide). (B) Simulated band structure of transverse electromagnetic modes of a straight topological waveguide. The gray region corresponds to bulk modes of the individual topological photonic crystals, and red lines represent modes within the bandgap corresponding to topological edge states. The adjacent panel shows the measured spectrum at the transmitted end of the waveguide. The red shaded region identifies the topological edge band. k_x , reciprocal wave vector; a , lattice constant. (C) Transmission spectrum at point L as a function of the excitation laser position.

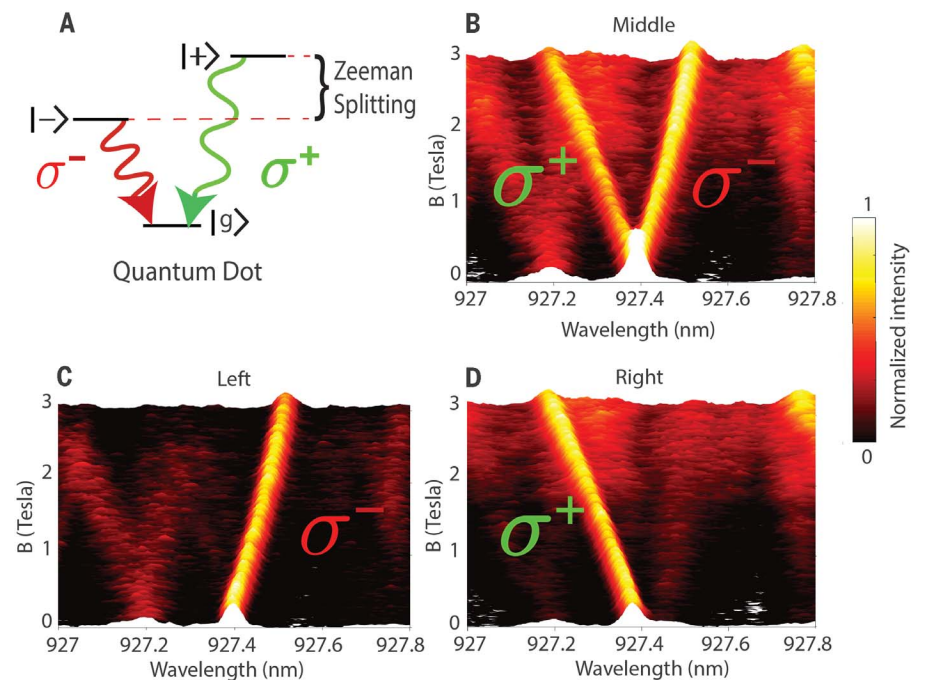


Fig. 3. Chirality in a straight topological waveguide. (A) Schematic of quantum dot-level structure in the presence of a magnetic field and radiative transitions with opposite circular polarizations. (B) Emission spectrum collected from the excitation region as a function of magnetic field (B). (C and D) Transmission spectra to left and right gratings, respectively.

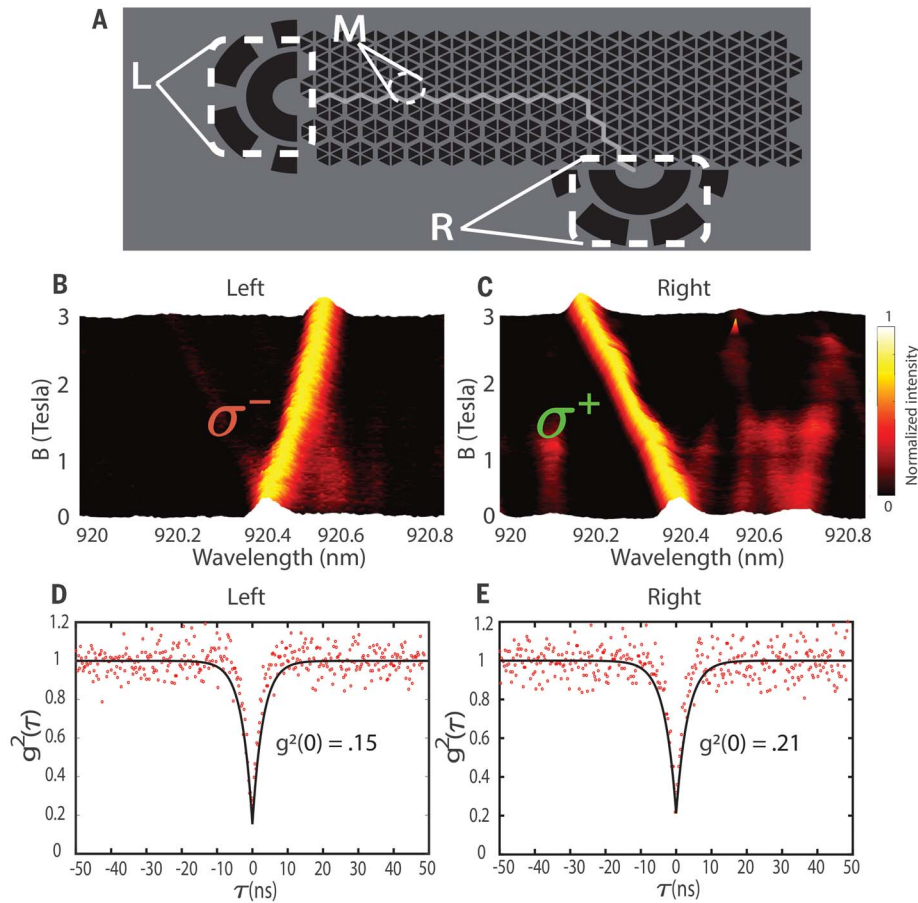


Fig. 4. Robust transport in two dimensions along a bend. (A) Schematic of a modified topological waveguide with a bend. (B and C) Photoluminescence collected from points L and R, respectively, showing only one branch of the quantum dot. (D and E) Second-order correlation measurement [$g^2(\tau)$, where τ is the time delay] data obtained from points L and R, respectively, showing antibunching. Red dots represent the experimental data, and the black line corresponds to fitting.

demonstrates an absence of back-reflection at the bend, which would result in a strong signal for both polarizations at the left grating. We also confirmed that these routed photons are single photons by performing a second-order correlation measurement for photons collected from both ends of the waveguide, which exhibits strong antibunching (Fig. 4, D and E). The robustness in this system is due to C_{6v} symmetry, and the boundary and disorder can break this symmetry and lead to backscattering of the edge modes. In the supplementary materials, we analyze the effect of certain types of disorder on the transmission properties of the edge modes and show that the unidirectional propagation is robust. The full characterization of robustness, beyond numerical simulations and the tight-binding model (26), requires further study.

In this work, we demonstrated coupling between single quantum emitters and topologically robust photonic edge states. Our approach opens new prospects at the interface of quantum optics and topological photonics. In the context of chiral quantum optics, one can explore new regimes of dipole emission in the vicinity of topological photonic structures and exploit the robustness of the electromagnetic modes (16). Furthermore, in a chiral waveguide, photon-mediated interactions between emitters are location-independent (27). This property could facilitate the coupling of multiple solid-state emitters via photons while overcoming scalability issues associated with random emitter position, enabling large-scale super-radiant states and spin-squeezing. Ultimately, such an approach could constitute a versatile platform to explore many-body quantum physics

at a topological edge (28), create chiral spin networks (27, 29), and realize fractional quantum Hall states of light (30, 31).

REFERENCES AND NOTES

1. J. Dalibard, F. Gerbier, G. Juzeliūnas, P. Öhberg, *Rev. Mod. Phys.* **83**, 1523–1543 (2011).
2. C. Eckardt, *Rev. Mod. Phys.* **89**, 011004 (2017).
3. M. Hafezi, J. M. Taylor, *Phys. Today* **67**, 68–69 (2014).
4. L. Lu, J. D. Joannopoulos, M. Soljačić, *Nat. Photonics* **8**, 821–829 (2014).
5. L. Kane, T. C. Lubensky, *Nat. Phys.* **10**, 39–45 (2014).
6. J. Paulose, B. G. G. Chen, V. Vitelli, *Nat. Phys.* **11**, 153–156 (2015).
7. R. Süsstrunk, S. D. Huber, *Science* **349**, 47–50 (2015).
8. Z. Wang, Y. Chong, J. D. Joannopoulos, M. Soljačić, *Nature* **461**, 772–775 (2009).
9. X. Cheng *et al.*, *Nat. Mater.* **15**, 542–548 (2016).
10. M. Hafezi, S. Mittal, J. Fan, A. Migdall, J. M. Taylor, *Nat. Photonics* **7**, 1001–1005 (2013).
11. M. C. Rechtsman *et al.*, *Nature* **496**, 196–200 (2013).
12. M. Hafezi, E. A. Demler, M. D. Lukin, J. M. Taylor, *Nat. Phys.* **7**, 907–912 (2011).
13. L. Pilozzi, C. Conti, *Phys. Rev. B* **93**, 195317 (2016).
14. G. Harari *et al.*, “Topological lasers,” in *Conference on Lasers and Electro-Optics* [OSA Technical Digest (online), Optical Society of America, 2016], FM3A.3.
15. P. St-Jean *et al.*, *Nat. Photonics* **11**, 651–656 (2017).
16. P. Lodahl *et al.*, *Nature* **541**, 473–480 (2017).
17. I. Carusotto, C. Ciuti, *Rev. Mod. Phys.* **85**, 299–366 (2013).
18. J. I. Cirac, H. J. Kimble, *Nat. Photonics* **11**, 18–20 (2017).
19. D. G. Angelakis, Ed., *Quantum Simulations with Photons and Polaritons* (Springer International Publishing, 2017).
20. L. H. Wu, X. Hu, *Phys. Rev. Lett.* **114**, 223901 (2015).
21. S. Barik, H. Miyake, W. DeGottardi, E. Waks, M. Hafezi, *New J. Phys.* **18**, 113013 (2016).
22. Materials and methods are available as supplementary materials.
23. M. Bayer *et al.*, *Phys. Rev. B* **65**, 195315 (2002).
24. J. Petersen, J. Volz, A. Rauschenbeutel, *Science* **346**, 67–71 (2014).
25. I. Söllner *et al.*, *Nat. Nanotechnol.* **10**, 775–778 (2015).
26. T. Kariyado, X. Hu, *Sci. Rep.* **7**, 16515 (2017).
27. H. Pichler, T. Ramos, A. J. Daley, P. Zoller, *Phys. Rev. A* **91**, 042116 (2014).
28. M. Ringel, M. Pletyukhov, V. Gritsev, *New J. Phys.* **16**, 113030 (2014).
29. A. Metelmann, A. Clerk, *Phys. Rev. X* **5**, 021025 (2015).
30. R. O. Umucallar, I. Carusotto, *Phys. Rev. Lett.* **108**, 206809 (2012).
31. M. Hafezi, M. D. Lukin, J. M. Taylor, *New J. Phys.* **15**, 063001 (2013).

ACKNOWLEDGMENTS

The authors acknowledge fruitful discussions with S. Mittal. All data needed to evaluate the conclusions are present in the paper and/or the supplementary materials. This research was supported by the Office of Naval Research, the Air Force Office of Scientific Research—Multidisciplinary University Research Initiative (grant FA9550-16-1-0323), the Sloan Foundation, and the Physics Frontier Center at the Joint Quantum Institute.

SUPPLEMENTARY MATERIALS

www.sciencemag.org/content/359/6376/666/suppl/DC1
Materials and Methods
Supplementary Text
Figs. S1 to S5
Table S1

24 September 2017; accepted 11 December 2017
10.1126/science.aarQ327

Materials and Methods

Device Fabrication

To fabricate the device, we began with an initial wafer composed of a 160 nm GaAs membrane on top of 1 μm sacrificial layer of Al_{0.8}Ga_{0.2}As with quantum dots grown at the center. The quantum dot density was approximately 50 μm^{-2} . Based on the given quantum density and cross-sectional area of the waveguide, the probability of finding two dots in the structure with the same resonance is less than 0.7%. Thus, it is extremely unlikely in a given device for a photon emitted by one dot to be scattered by a second.

We fabricated the topological photonic crystal structure using electron beam lithography, followed by dry etching and selective wet etching of the sacrificial layer. We first spin-coated the wafer with ZEP520A e-beam resist, then patterned the structure using 100 keV acceleration voltage and developed the resist using ZED50 developer. After patterning, we used chlorine-based inductively coupled plasma etching to transfer the pattern on the GaAs membrane. We finally performed selective wet etching using HF to create a suspended structure with air on top and bottom. The rectangular structures in the periphery are included to facilitate undercut of the sacrificial layer.

Sharp corners with straight side walls are essential to observe the topological helical edge modes. It is confirmed via simulation that triangles with rounded corners are detrimental for the device operation. However, even with highly directional dry etch, creating sharp features like triangles is challenging at such small length scales. We observed – by using a regular mask design (as shown in Figure S1.A) – that etching causes widening of holes which eventually results in rounded corners much like a Reuleaux triangle (Figure S1.B). We used a modified mask design to overcome this challenge. Triangles with shrunk edges shown in Figure S1.C are used as a mask; this results in sharp triangles with edge lengths of 140 nm. Close up SEM image of final structure is shown in Figure S1.D.

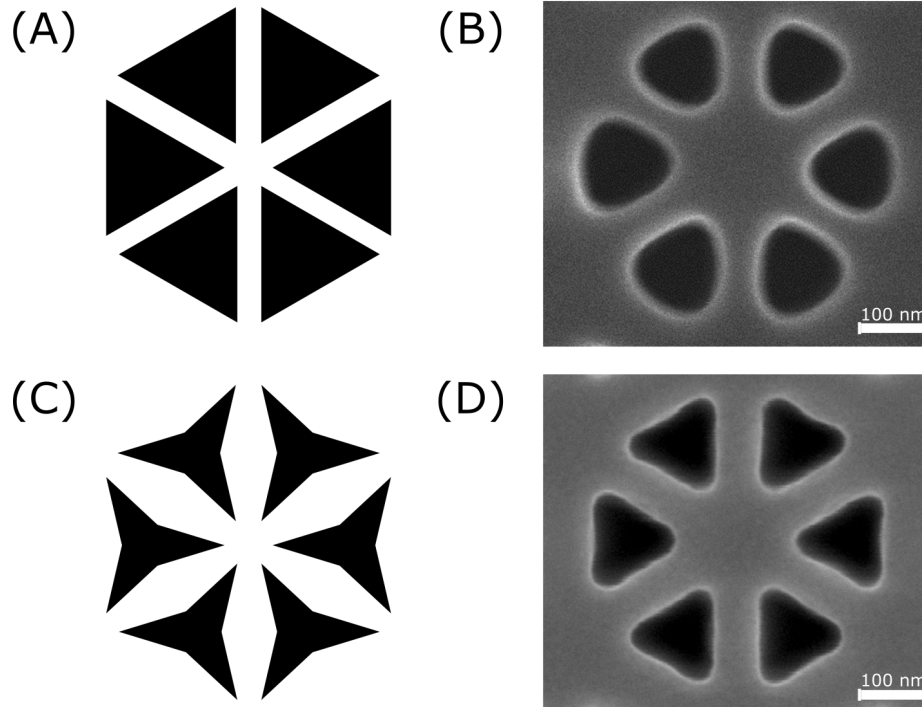


Figure S1. Mask design for fabrication of triangles. (A) Layout of regular mask. (B) SEM image of rounded triangles resulted from use of regular mask. (C) Layout of modified mask; triangles are bent from edges to mitigate etching imperfections. (D) SEM image of sharp triangles fabricated with use of modified mask.

Experimental Setup

To perform measurements, we mounted the sample in a closed-cycle cryostat and cooled it down to 3.6 K. A superconducting magnet, contained within the closed-cycle refrigerator, surrounds the sample and applies a magnetic field of up to 9.2 T along the out-of-plane (Faraday) direction in order to generate a Zeeman splitting between the two bright excitons of the quantum dot. We performed all sample excitation and collection using a confocal microscope with an objective lens with numerical aperture of 0.8. We collected the emission and focused it onto a single mode fiber to perform spatial filtering. To perform spectral measurements, we injected the signal to a grating spectrometer with a spectral resolution of 7 GHz. For autocorrelation measurements, we used a flip mirror to couple the light out of the spectrometer and processed the filtered emission using Hanbury-Brown Twiss intensity interferometer composed of a 50/50 beamsplitter, two Single Photon Counting Modules (SPCMs) and a PicoHarp 300 time correlated single photon counting system.

The quantum dots are less than 20 nm in diameter, while the laser spot size is approximately 0.4 μm . The density of quantum dots are 50 μm^{-2} , which means that there are approximately 25 dots within the excitation spots. However, due to the large

inhomogeneous broadening of the ensemble, each of these dots emits at a different wavelength. We isolate individual quantum dots by spectral filtering using a grating spectrometer with a resolution of 0.02 nm. The spectrometer selects the emission from only a single dot, as evidenced by the anti-bunching dip observed in Fig. 4D-E which dips below 0.5.

Supplementary Text

Device Design

Figure S2 shows a schematic of the device design. We begin with a honeycomb lattice of equilateral triangles exhibiting hexagonal symmetry as our baseline structure. This lattice is a triangular lattice of cells consisting of six equilateral triangular holes, indicated by the dashed line. We use a lattice constant of $a_0 = 445$ nm, an edge length of the equilateral triangle of $s = 140$ nm, and a slab thickness of $h = 160$ nm. R defines the distance from the center of a cell to the centroid of a triangle. In this structure a perfect honeycomb lattice corresponds to $R = a_0/3$.

With these parameters we obtain doubly degenerate Dirac cones at 319 THz (940 nm). We form the two mirrors by concentrically expanding or contracting the unit cell.

We create topologically distinct regions by deforming the unit cell of the pristine honeycomb lattice. In the blue region in Figure 1A, we concentrically shift the triangular holes by increasing R to $1.05a_0/3$, thereby shifting all the triangular holes in an individual cell outward. This deformation results in the band structure shown in Figure 1C. In the yellow region, we decrease R to $0.94a_0/3$, which pulls the holes towards the center resulting in the band structure shown in Figure 1D.

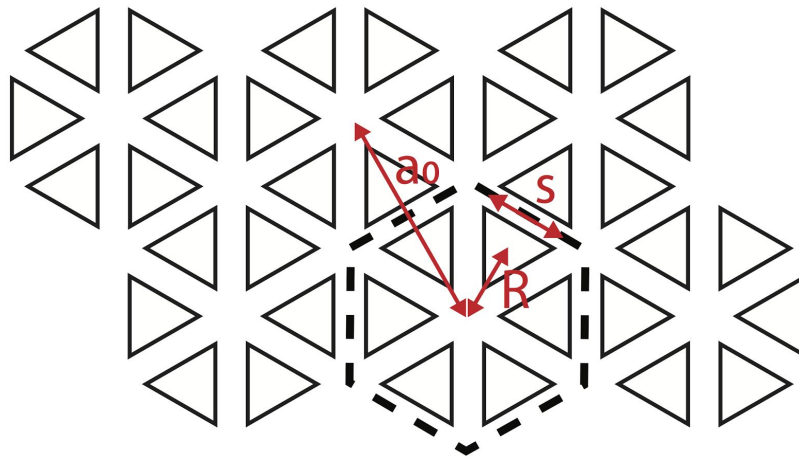


Figure S2. Design of honeycomb-like photonic crystal.

Symmetry-Protected Topological Photonic Crystal

Once thought to be limited to the quantum Hall effect, the notion of topological insulating phases has revolutionized condensed matter physics and is the inspiration for topological photonic systems. These states are based on the fact that insulating Hamiltonians which obey certain combinations of symmetries (such as time-reversal) can be classified according to their topology. The photonic crystal considered here is described by a Z_2 topological invariant, which takes the value 0 (trivial phase) or 1 (topological phase). The physical manifestation of this is that between regions of differing topology, protected edge modes are found. These modes cannot be coupled since such a term would violate the protected symmetry.

The photonic crystal considered in this work is an analog of a quantum spin Hall system for photons and is discussed in greater detail in (20, 21). The quantum spin Hall system exhibits topological protection that is based on time-reversal symmetry. In the context of the photonic crystal, the role of time-reversal symmetry is played by the six-fold rotational (C_{6v}) crystal symmetry of the hexagonal unit cell. In the energy range of interest, the band structure of the system is described by the Dirac equation, where the mass is controlled by the spacing of triangles in a hexagonal cluster. The topological Z_2 index reflects the sign of the mass, and is positive (negative) for compressed (expanded) regions. The topologically protected counterpropagating modes exist in the region at which the mass changes sign. In the context of the Dirac equation, these states are known as Jackiw-Rebbi states (21).

The yellow and blue regions in Figure 1A represent the topologically distinct phases discussed above. Topological modes exist at the boundary, and are protected from any disorder which respects the six-fold crystal symmetry. Disorder that breaks this symmetry can lead to the backscattering of the edge modes. In fact, the formation of the interface itself can break this symmetry, albeit weakly. Through extensive simulations, we have found that the zig-zag interface in our device adequately preserves the crystalline symmetry, thereby minimizing the coupling between the counterpropagating edge modes. Figure S3.A shows the propagating mode for this interface, while Figure S3.B shows the propagation length of the waveguide as a function of wavelength. The simulated propagation length is approximately $22 \mu\text{m}$. We note that although this propagation length is longer than our device ($15 \mu\text{m}$), it is short compared to a conventional photonic crystal waveguide. This reduced propagation length is due to the fact that we are forming a guided mode from a perturbed hexagonal lattice. In the pure hexagonal lattice all modes exist below the light line (21), but after perturbation the structure exhibits a triangular rather than hexagonal symmetry. This change in symmetry can cause modes to scatter to the Γ point which is above the light line. Using a progressively weaker perturbation leads to less scattering, and therefore longer propagation lengths (Figure S3.C), which must be traded off with a narrower topological bandgap. In Figure S3.D, we show simulations illustrating the robustness of the edge modes to a certain type of defect. The defect, an entire missing cell, breaks C_{6v} crystal

symmetry. However, this defect does not adversely affect the transmission in the gapped region. We should note that the disorder seen in our device is considerably less severe.

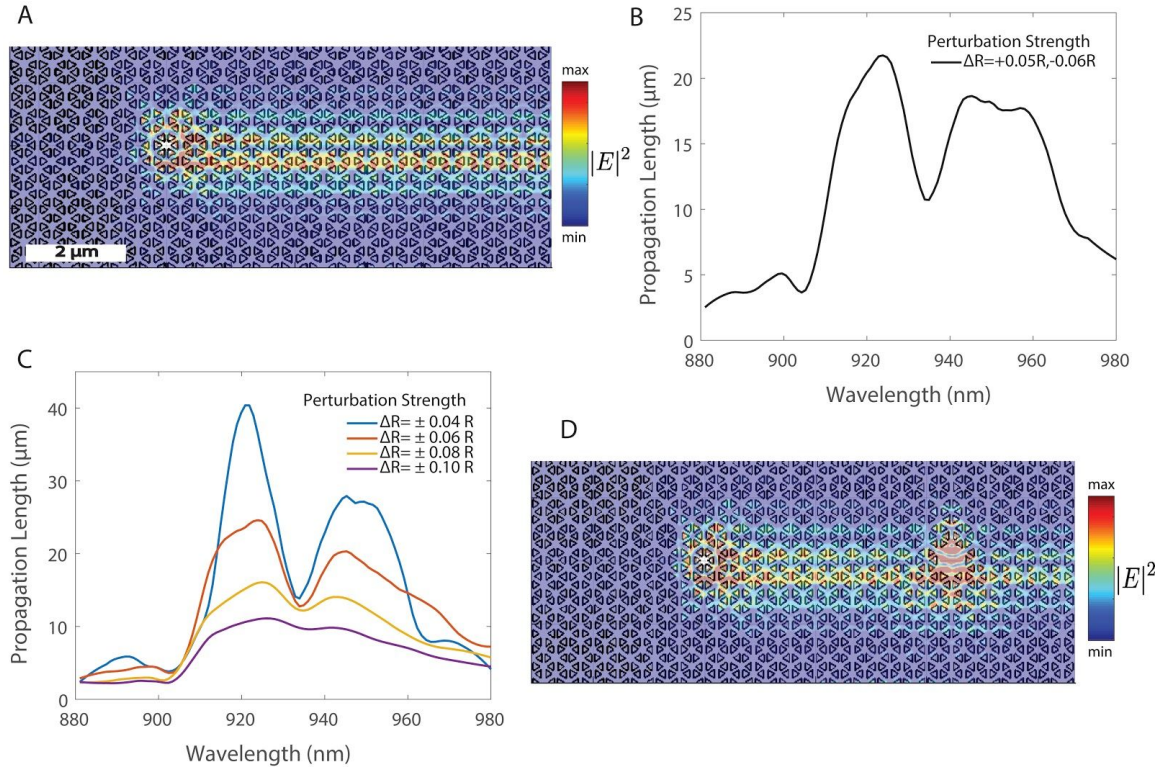


Figure S3. Propagation loss and robustness of edge modes. (A) Simulation showing electric field intensity for propagation of edge state in a topological waveguide without a defect (B) Propagation length for the edge state in our measured device. The perturbation parameter is $\Delta R = R_0 - R_{\text{in/out}}$, where R is defined as in Fig S2. The parameter R_0 corresponds to the unperturbed original honeycomb lattice, and $R_{\text{in/out}}$ characterize the inward/outward perturbed lattices, respectively. (C) Simulation results showing propagation lengths of edge states in the topological photonic crystal waveguide as we change ΔR . (D) Simulation showing electric field intensity of edge states as it propagates around a defect.

Grating Calibration

Since both left and right grating couplers are fabricated under similar condition they are identical in terms of coupling efficiency. To test this fact we calibrated them with respect to. the transmission spectrum of the topological waveguide. Figure S4.A shows the different positions on the device. We shine an intense excitation beam of 780 nm with 1.5uW power at the center of the waveguide (M). At this high power all the quantum dots are saturated and emit a broadband spectrum ranging from 900-980nm. We collected the transmitted signal from left (L) and right grating (R). Figure S4.B shows almost equal counts coming from both the gratings with almost overlapping transmission spectrum. Additionally, the area under the curves give approximately 40 million counts/sec for the gratings thus indicating equal coupling efficiency.

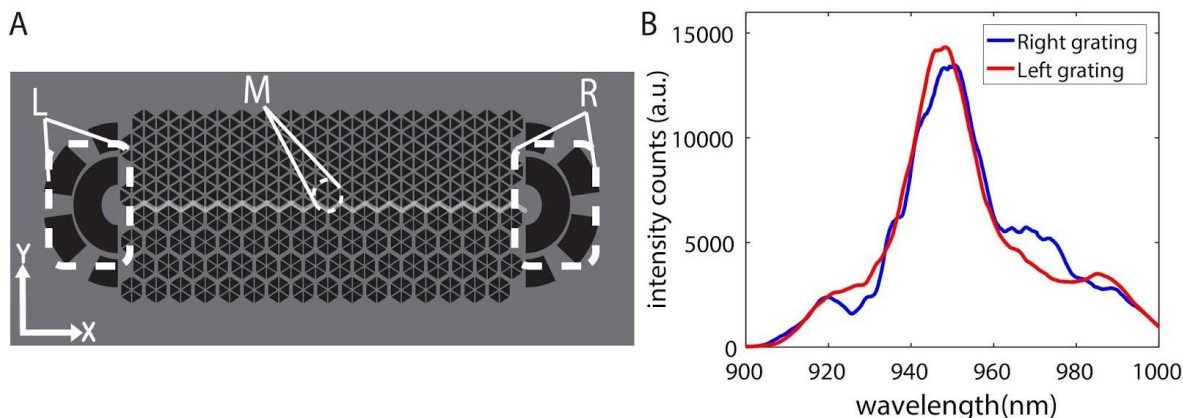


Figure S4. Transmission data from left and right gratings. (A) Scheme for excitation and collection. (B) Transmitted signal collected from two gratings.

Polarization of Quantum Dots in Bulk Under Magnetic Field

We first measured the photoluminescence from a bare QD in the bulk. With the application of magnetic field QD emission spectrum splitted into two branches with circularly polarized emission as shown in Figure S5. A and denoted by σ^\pm . At a very high magnetic field of 3T the separation between two branches becomes 0.3nm. at this stage to verify the selection rules we introduced a quarter wave plate and a polarizer before collecting the signal. Figure S5.B shows recorded photoluminescence obtained by rotating the polarizer angle. The antiphase relation between the two branches along with the detection scheme confirms that they are indeed circularly polarized in bulk under high magnetic field.

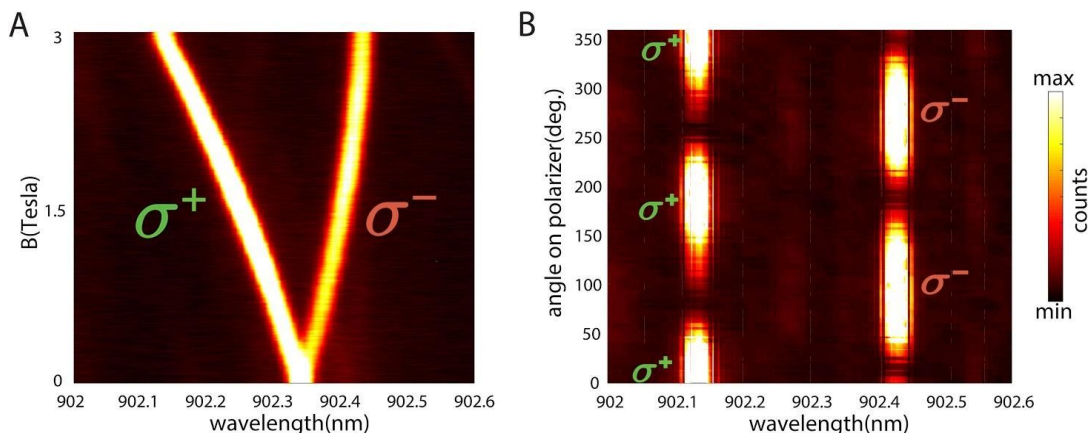


Figure S5. Polarization of quantum dot emission in bulk under magnetic field. (A) Splitting of single QD emission into σ^+ and σ^- exciton branches under application of magnetic field. (B) Verification of circular polarization of excitonic branches with polarization selective photoluminescence.

Coupling Efficiency

The coupling efficiency of emission from a single quantum emitter into the topological

waveguide is defined by $\beta = \frac{I_L + I_R}{I_L + I_R + I_M}$ where I_L and I_R are the integrated photon counts propagating to the left and right waveguide modes respectively, and I_M is the photon counts emitted directly from the middle of the device into free space. We can estimate these intensities by measuring the brightness at the three locations denoted in the main text. Table S1 shows the coupling efficiencies calculated for different dots coupled to our topological device. The table reports integrated count rates for an integration time of 1s at each point. We determine the average to be 68%. If we take the estimated propagation loss into account (from Fig S3.B), the coupling efficiency will be higher at ~75%.

Coupled QDs	I_M	I_L	I_R	(%)
1	699	772	740	77.98
2	655	755	735	88.89
3	680	780	780	84.93
4	1300	1400	1900	75.23
5	802	1080	933	81.17
6	739	1021	654	78.85
7	795	1206	645	77.95
8	1090	1061	724	53.50
9	976	934	667	50.00
10	677	1079	807	92.44
11	869	728	819	54.90
12	1531	809	986	37.56
13	884	716	700	39.06
			<i>Avg</i>	68.65

Table S1. Estimation of coupling efficiency.

References and Notes

1. J. Dalibard, F. Gerbier, G. Juzeliūnas, P. Öhberg, Colloquium: Artificial gauge potentials for neutral atoms. *Rev. Mod. Phys.* **83**, 1523–1543 (2011). [doi:10.1103/RevModPhys.83.1523](https://doi.org/10.1103/RevModPhys.83.1523)
2. C. Eckardt, Atomic quantum gases in periodically driven optical lattices. *Rev. Mod. Phys.* **89**, 011004 (2017). [doi:10.1103/RevModPhys.89.011004](https://doi.org/10.1103/RevModPhys.89.011004)
3. M. Hafezi, J. M. Taylor, Topological physics with light. *Phys. Today* **67**, 68–69 (2014). [doi:10.1063/PT.3.2394](https://doi.org/10.1063/PT.3.2394)
4. L. Lu, J. D. Joannopoulos, M. Soljačić, Topological photonics. *Nat. Photonics* **8**, 821–829 (2014). [doi:10.1038/nphoton.2014.248](https://doi.org/10.1038/nphoton.2014.248)
5. L. Kane, T. C. Lubensky, Topological boundary modes in isostatic lattices. *Nat. Phys.* **10**, 39–45 (2014). [doi:10.1038/nphys2835](https://doi.org/10.1038/nphys2835)
6. J. Paulose, B. G. G. Chen, V. Vitelli, Topological modes bound to dislocations in mechanical metamaterials. *Nat. Phys.* **11**, 153–156 (2015). [doi:10.1038/nphys3185](https://doi.org/10.1038/nphys3185)
7. R. Süsstrunk, S. D. Huber, Observation of phononic helical edge states in a mechanical topological insulator. *Science* **349**, 47–50 (2015). [doi:10.1126/science.aab0239](https://doi.org/10.1126/science.aab0239) [Medline](#)
8. Z. Wang, Y. Chong, J. D. Joannopoulos, M. Soljačić, Observation of unidirectional backscattering-immune topological electromagnetic states. *Nature* **461**, 772–775 (2009). [doi:10.1038/nature08293](https://doi.org/10.1038/nature08293) [Medline](#)
9. X. Cheng, C. Jouvaud, X. Ni, S. H. Mousavi, A. Z. Genack, A. B. Khanikaev, Robust reconfigurable electromagnetic pathways within a photonic topological insulator. *Nat. Mater.* **15**, 542–548 (2016). [doi:10.1038/nmat4573](https://doi.org/10.1038/nmat4573) [Medline](#)
10. M. Hafezi, S. Mittal, J. Fan, A. Migdall, J. M. Taylor, Imaging topological edge states in silicon photonics. *Nat. Photonics* **7**, 1001–1005 (2013). [doi:10.1038/nphoton.2013.274](https://doi.org/10.1038/nphoton.2013.274)
11. M. C. Rechtsman, J. M. Zeuner, Y. Plotnik, Y. Lumer, D. Podolsky, F. Dreisow, S. Nolte, M. Segev, A. Szameit, Photonic Floquet topological insulators. *Nature* **496**, 196–200 (2013). [doi:10.1038/nature12066](https://doi.org/10.1038/nature12066) [Medline](#)
12. M. Hafezi, E. A. Demler, M. D. Lukin, J. M. Taylor, Robust optical delay lines with topological protection. *Nat. Phys.* **7**, 907–912 (2011). [doi:10.1038/nphys2063](https://doi.org/10.1038/nphys2063)
13. L. Pilozzi, C. Conti, Topological lasing in resonant photonic structures. *Phys. Rev. B* **93**, 195317 (2016). [doi:10.1103/PhysRevB.93.195317](https://doi.org/10.1103/PhysRevB.93.195317)
14. G. Harari, M. A. Bandres, Y. Lumer, Y. Plotnik, D. N. Christodoulides, M. Segev, “Topological lasers,” in *Conference on Lasers and Electro-Optics* [OSA Technical Digest (online), Optical Society of America, 2016], FM3A.3.
15. P. St-Jean, V. Goblot, E. Galopin, A. Lemaître, T. Ozawa, L. Le Gratiet, I. Sagnes, J. Bloch, A. Amo, Lasing in topological edge states of a one-dimensional lattice. *Nat. Photonics* **11**, 651–656 (2017). [doi:10.1038/s41566-017-0006-2](https://doi.org/10.1038/s41566-017-0006-2)

16. P. Lodahl, S. Mahmoodian, S. Stobbe, A. Rauschenbeutel, P. Schneeweiss, J. Volz, H. Pichler, P. Zoller, Chiral quantum optics. *Nature* **541**, 473–480 (2017).
[doi:10.1038/nature21037](https://doi.org/10.1038/nature21037) [Medline](#)
17. I. Carusotto, C. Ciuti, Quantum fluids of light. *Rev. Mod. Phys.* **85**, 299–366 (2013).
[doi:10.1103/RevModPhys.85.299](https://doi.org/10.1103/RevModPhys.85.299)
18. J. I. Cirac, H. J. Kimble, Quantum optics, what next? *Nat. Photonics* **11**, 18–20 (2017).
[doi:10.1038/nphoton.2016.259](https://doi.org/10.1038/nphoton.2016.259)
19. D. G. Angelakis, Ed., *Quantum Simulations with Photons and Polaritons* (Springer International Publishing, 2017).
20. L. H. Wu, X. Hu, Scheme for achieving a topological photonic crystal by using dielectric material. *Phys. Rev. Lett.* **114**, 223901 (2015). [doi:10.1103/PhysRevLett.114.223901](https://doi.org/10.1103/PhysRevLett.114.223901)
[Medline](#)
21. S. Barik, H. Miyake, W. DeGottardi, E. Waks, M. Hafezi, Two-dimensionally confined topological edge states in photonic crystal. *New J. Phys.* **18**, 113013 (2016).
[doi:10.1088/1367-2630/18/11/113013](https://doi.org/10.1088/1367-2630/18/11/113013)
22. Materials and methods are available as supplementary materials.
23. M. Bayer, G. Ortner, O. Stern, A. Kuther, A. A. Gorbunov, A. Forchel, P. Hawrylak, S. Fafard, K. Hinzer, T. L. Reinecke, S. N. Walck, J. P. Reithmaier, F. Klopff, F. Schäfer, Fine structure of neutral and charged excitons in self-assembled In(Ga)As/(Al)GaAs quantum dots. *Phys. Rev. B* **65**, 195315 (2002). [doi:10.1103/PhysRevB.65.195315](https://doi.org/10.1103/PhysRevB.65.195315)
24. J. Petersen, J. Volz, A. Rauschenbeutel, Chiral nanophotonic waveguide interface based on spin-orbit interaction of light. *Science* **346**, 67–71 (2014). [doi:10.1126/science.1257671](https://doi.org/10.1126/science.1257671)
[Medline](#)
25. I. Söllner, S. Mahmoodian, S. L. Hansen, L. Midolo, A. Javadi, G. Kiršanskė, T. Pregnolato, H. El-Ella, E. H. Lee, J. D. Song, S. Stobbe, P. Lodahl, Deterministic photon-emitter coupling in chiral photonic circuits. *Nat. Nanotechnol.* **10**, 775–778 (2015).
[doi:10.1038/nnano.2015.159](https://doi.org/10.1038/nnano.2015.159) [Medline](#)
26. T. Kariyado, X. Hu, Topological states characterized by mirror winding numbers in graphene with bond modulation. *Sci. Rep.* **7**, 16515 (2017). [doi:10.1038/s41598-017-16334-0](https://doi.org/10.1038/s41598-017-16334-0)
[Medline](#)
27. H. Pichler, T. Ramos, A. J. Daley, P. Zoller, Quantum optics of chiral spin networks. *Phys. Rev. A* **91**, 042116 (2014). [doi:10.1103/PhysRevA.91.042116](https://doi.org/10.1103/PhysRevA.91.042116)
28. M. Ringel, M. Pletyukhov, V. Gritsev, Topologically protected strongly correlated states of photons. *New J. Phys.* **16**, 113030 (2014). [doi:10.1088/1367-2630/16/11/113030](https://doi.org/10.1088/1367-2630/16/11/113030)
29. A. Metelmann, A. A. Clerk, Nonreciprocal photon transmission and amplification via reservoir engineering. *Phys. Rev. X* **5**, 021025 (2015). [doi:10.1103/PhysRevX.5.021025](https://doi.org/10.1103/PhysRevX.5.021025)
30. R. O. Umucalılar, I. Carusotto, Fractional quantum Hall states of photons in an array of dissipative coupled cavities. *Phys. Rev. Lett.* **108**, 206809 (2012).
[doi:10.1103/PhysRevLett.108.206809](https://doi.org/10.1103/PhysRevLett.108.206809) [Medline](#)

31. M. Hafezi, M. D. Lukin, J. M. Taylor, Non-equilibrium fractional quantum Hall state of light. *New J. Phys.* **15**, 063001 (2013). [doi:10.1088/1367-2630/15/6/063001](https://doi.org/10.1088/1367-2630/15/6/063001)